Geochemistry, Geophysics, Geosystems®

AGU ADVANCING EARTH AND SPACE SCIENCES

RESEARCH ARTICLE
10.1029/2024GC011913

B-Type Olivine Fabrics Within the Cumulate Buck Creek Ultramafic Body Emplaced During Southern Appalachian Taconic Subduction

Virginia L. Peterson[1], Jeffrey M. Rahl[2], Samuel DeYoung[3], Davis Eyth[4], Madeline Mennenga[5], and Benjamin A. Pummell[6]

[1]Geology Department, Grand Valley State University, Allendale, MI, USA, [2]Department of Earth and Environmental Geoscience, Washington and Lee University, Lexington, VA, USA, [3]ERM, Holland, MI, USA, [4]GHD, Plainwell, MI, USA, [5]SES Environmental, Grandville, MI, USA, [6]Department of Earth and Environmental Sciences, Syracuse University, Syracuse, NY, USA

Key Points:

- Cumulate dunites emplaced in Appalachian Taconic subduction preserve B-type olivine crystallographic preferred orientations
- Dunites deformed under lower stress and water content than experimental B-type conditions
- Olivine textures consistent with dislocation creep and minor grain-boundary sliding

Supporting Information:

Supporting Information may be found in the online version of this article.

Correspondence to:

V. L. Peterson,
petersvi@gvsu.edu

Citation:

Peterson, V. L., Rahl, J. M., DeYoung, S., Eyth, D., Mennenga, M., & Pummell, B. A. (2025). B-type olivine fabrics within the cumulate Buck Creek ultramafic body emplaced during southern Appalachian Taconic subduction. *Geochemistry, Geophysics, Geosystems*, *26*, e2024GC011913. https://doi.org/10.1029/2024GC011913

Received 30 SEP 2024
Accepted 24 MAR 2025

Author Contributions:

Conceptualization: Virginia L. Peterson, Jeffrey M. Rahl
Formal analysis: Virginia L. Peterson, Jeffrey M. Rahl, Samuel DeYoung, Davis Eyth, Madeline Mennenga, Benjamin A. Pummell
Funding acquisition: Virginia L. Peterson, Madeline Mennenga
Investigation: Virginia L. Peterson, Jeffrey M. Rahl, Samuel DeYoung, Davis Eyth, Madeline Mennenga, Benjamin A. Pummell

Abstract The Buck Creek ultramafic complex is a fragment of oceanic cumulate emplaced into the lower Laurentian continental crust during Ordovician Taconic subduction. We document olivine fabrics in the relatively pristine dunites preserved from peak metamorphic conditions of ~850°C and 1.0–1.4 GPa confining pressure. Mineral assemblages and microstructures indicate nearly anhydrous conditions at peak metamorphism and the activity of dislocation creep with minor evidence of grain boundary sliding. Grain size piezometry indicates stress conditions of ~17–25 MPa. Analysis of crystallographic preferred orientations (CPO) and intracrystalline misorientations indicate the primary activity of the [001](010) slip system leading to the development of B-type olivine fabrics. We suggest that the Buck Creek dunites formed as ocean crust cumulates and were partially subducted beneath the Laurentian continental crust to deformation conditions similar to those in the shallow mantle wedge. We document that deformation at Buck Creek occurred at lower differential stress conditions and lower water content than typically associated with B-type CPOs, broadening the range of known conditions in which these fabrics may form.

Plain Language Summary Olivine is the most abundant mineral in the Earth's upper mantle, and its mechanical behavior influences important processes, including plate tectonics. Previous research finds that when rocks are squeezed deep within the Earth, an alignment of olivine crystal axes, referenced as "fabric," can be produced that varies with pressure, temperature, water content, and other factors. In this work, we document the fabric in olivine-rich rocks of the Buck Creek ultramafic complex, a large fragment of oceanic crust exposed in the southern Appalachians. We show the development of a particular crystal fabric style (B-type) that formed at lower stress conditions and water content than predicted by most experimental work. This finding is important because it expands our knowledge of the olivine deformation style in the natural world, informing our understanding of deep Earth processes.

1. Introduction

Our understanding of the relationship between olivine crystallographic preferred orientation (CPO) and plastic deformation of mantle rocks has expanded significantly through experimental and natural studies of peridotites. Experimental work documents distinctive olivine CPO types (termed A, B, C, D, E, AG) (Figure 1a inset) defined by characteristic alignments of [100], [010], and [001] with respect to a kinematic reference frame (strain X-Y-Z). These distinct CPO types develop through the activity of specific slip systems that dominate at particular deformation conditions: temperature, differential stress, water content, pressure, deformation mechanisms, presence of melt, and the geometry of finite strain (Carter & Ave'Lallemant, 1970; Chatzaras et al., 2016; Jung, Mo, & Green, 2009; Jung et al., 2006; Karato et al., 2008; Kohlstedt & Holtzman, 2009; Nicolas et al., 1973; Précigout & Hirth, 2014).

Ideally, these experimentally constrained olivine CPO types would be well-linked to tectonic settings such that natural patterns provide clues to deformation conditions and seismic anisotropy within the mantle. Accordingly, efforts to document natural olivine deformation conditions have focused on mantle xenoliths (Behr & Smith, 2016; Chatzaras et al., 2016; Jung, Mo, & Choi, 2009; Lee & Jung, 2015) as well as in situ, tectonically emplaced ultramafic bodies (Cao et al., 2017; Drury et al., 2011; Jung, 2009; Jung et al., 2014; Mizukami

Resources: Virginia L. Peterson, Jeffrey M. Rahl
Software: Jeffrey M. Rahl, Madeline Mennenga
Supervision: Virginia L. Peterson
Writing – original draft: Virginia L. Peterson
Writing – review & editing: Virginia L. Peterson, Jeffrey M. Rahl, Samuel DeYoung, Davis Eyth, Madeline Mennenga, Benjamin A. Pummell

et al., 2004; Précigout & Hirth, 2014; Skemer et al., 2006; Tasaka et al., 2008; Webber et al., 2008). In a recent review of natural olivine deformation data, Bernard et al. (2019) showed that formation conditions for natural olivine CPO types are not well correlated with experimental constraints, particularly when extrapolated to lower stress magnitudes and water contents (Figure 1a). At these lower stresses and strain rates, the CPO type may depend more on factors such as strain geometry, strain path, or deformation mechanisms than on deformation conditions. Most peridotites from the shallow, water-depleted continental and oceanic lithosphere preserve A-type fabrics (Bernard et al., 2019), the most commonly observed olivine CPO, which develops by dominant slip on the (010) plane in the direction of [100]. Experimental and natural constraints show that A-type fabrics form under conditions of low water contents (<700 ppm H/10^6 Si) and stress magnitude (Figure 1a) (Bernard et al., 2019), consistent with this shallow lithospheric setting.

We focus on the less common B-type fabrics formed by slip on the (010) plane in the direction of [001]. Experimental studies at high temperatures (1470–1570 K) (Jung et al., 2006; Karato et al., 2008) indicate that B-type fabrics typically develop under conditions of relatively high stress (>300 MPa) and high water content (>500 ppm H/10^6 Si) (Figure 1a). In water-saturated experiments, decreasing stress and temperature produces a transition from B- to C-type fabrics (Katayama & Karato, 2006) (Figure 1b). In natural samples, B-type fabrics have been documented in a wider range of settings, including some with significantly lower water content and stress conditions than predicted by experimental data (Bernard et al., 2019). B-type fabrics in olivine with low water content have also been associated with higher pressures deeper in the mantle (Lee & Jung, 2015; Précigout & Hirth, 2014). Similar to other CPO types, finite strain, strain history, and deformation mechanisms may significantly influence the formation of B-type fabrics in natural samples (e.g., Bernard et al., 2019). For example, diamond-bearing peridotites from South Africa (Lee & Jung, 2015) and mantle xenoliths from West Antarctica (Chatzaras et al., 2016) document a link between B-type fabrics and oblate finite strain.

Numerical modeling (Kneller et al., 2005, 2007) and observations in naturally deformed samples suggest that B-type slip during corner flow above older and colder subducting slabs under relatively wet, low stress conditions (Cao et al., 2015, 2017) may explain observations of seismically fast directions parallel to the trench. Thus, data from in situ ultramafic bodies tectonically emplaced above a subduction zone are critical to refining the range of conditions and history of deformation that form and preserve B-type fabrics. Existing studies from in situ bodies have identified B-type fabrics in a variety of tectonic settings. For example, some B-type fabrics, such as from the Bergen arc and Western Gneiss Region in Norway (Jung et al., 2014; Kim & Jung, 2015), the Swiss and Italian Alps (Jung, 2009; Skemer et al., 2006), and the Sangabawa belt (Tasaka et al., 2008), developed in relatively low stress, low temperature, and hydrous conditions consistent with formation in the shallow subduction wedge. In other instances, the B-type fabrics are associated instead with compaction of a crystal mush in a cumulate magma chamber setting (Cao et al., 2017; Yao et al., 2019). Strain history is also a factor; grain-size sensitive deformation mechanisms (e.g., grain-boundary sliding) are suggested to explain B-type fabrics preserved in the Ronda massif, Spain (Précigout & Hirth, 2014). In the Red Hills, New Zealand, B-type fabrics may be the result of resetting a pre-existing fabric (Webber et al., 2008, 2010).

"Alpine-type" ultramafic bodies exposed along the trend of the Appalachian Mountains represent an ideal target for documenting olivine fabrics emplaced above a subduction zone. These bodies form a discontinuous chain to the southeast of ~1.0 Ga basement massifs (Hibbard et al., 2006; Larabee, 1966), and the Blue Ridge of the southern Appalachians hosts numerous small and lenticular ultramafic bodies (Misra & Keller, 1978) emplaced during the early Paleozoic Taconic Orogeny. Many of these bodies are predominantly dunite with pristine olivine (Raymond et al., 2003).

We focus on the exceptionally well-characterized Buck Creek ultramafic body exposed in southwestern North Carolina (Figure 2a), the largest of the southern Appalachian ultramafic bodies. The Buck Creek body, comprised of mostly dunite interlayered with meta-troctolite, is enclosed within the Chunky Gal mafic complex (McElhaney & McSween, 1983) (Figure 2b). Field relationships and geochemistry indicate that the Buck Creek-Chunky Gal ultramafic-mafic complex formed as a mid-ocean-ridge cumulate (Peterson et al., 2009), likely Cambrian—Ordovician Iapetus oceanic crust. Sapphirine-bearing symplectite assemblages within the meta-troctolite suggest nearly anhydrous peak metamorphic conditions of ~850°C and 0.9–1.0 GPa (Lang et al., 2004; Tenthorey et al., 1996). Localized hydration along the margins of the meta-troctolite bodies created corundum-kyanite-zoisite assemblages consistent with formation at ~825°C and 1.1–1.4 GPa, similar to peak metamorphic

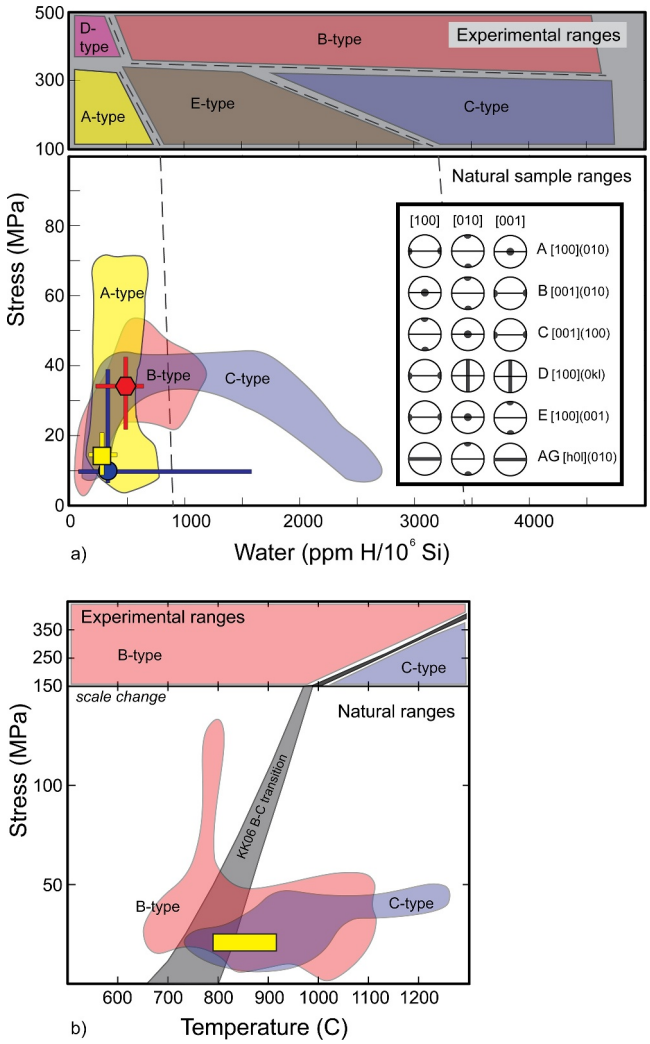

Figure 1. Graphs showing the range of common olivine deformation types for experimental and natural samples, adapted from Bernard et al. (2019). Inset: Typical CPO patterns of principal crystallographic axes for each deformation type shown on lower hemisphere equal area nets, adapted from Chatzaras et al. (2016). (a) Graph of water content versus stress. The higher stress region of the graph (above 100 MPa) shows shaded ranges of experimental conditions for CPO A–E-type olivine based on data from Jung et al. (2006) with dashed-line boundaries projected to lower stresses. Lower stress region shows range of natural published CPO A–C-types from Figure 7 of Bernard et al. (2019); shaded regions encompass their plotted data points for each type (A = yellow, B = red, C = blue). Solid symbols in darker colors with error bars represent median and lower quartile ranges for each type. (b) Graph of temperature versus stress illustrating conditions for B- to C-type transition, adapted from Figure 8a of Bernard et al. (2019). Higher stress experimental ranges and the KK06 B—C transition to lower stress from Katayama and Karato (2006). Shaded red and blue regions show the range of natural B- and C-type samples of Bernard et al. (2019). Yellow rectangle shows approximate deformation conditions for Buck Creek samples in this study.

conditions (Emilio, 1998), and overlapping with peak Taconic granulite-facies conditions of ~850°C at 0.7–0.9 GPa at 458 ± 1 Ma documented at Winding Stair Gap (WSG—Figure 2a) (El-Shazly, AK et al., 2011; Moecher et al., 2004). Peterson et al. (2009) suggested that the Buck Creek-Chunky Gal complex was subducted to depths of >30 km under dry conditions; localized hydration near peak pressures facilitated emplacement into the lower continental crust during the Taconic orogenic event. The complex is bounded by the Chunky Gal Mountain fault and experienced multiple stages of regional deformation related to continuing convergence that culminated in the collision of Gondwana with Laurentia (Hatcher, 1978; Lacazette & Rast, 1989; McElhaney & McSween, 1983; Peterson et al., 2009).

We make a case that the Buck Creek cumulate olivine, emplaced in a subduction zone setting into the lower Laurentian crust, preserves B-type fabrics developed in the region of the Taconic subduction wedge under conditions of relatively low stress, low temperature and low water content, broadening constraints on the evolution of these fabrics in a well-characterized natural setting.

2. Materials and Methods

2.1. Field and Sampling Methods

Sampling for this study was guided by detailed maps created by Hadley (1949) and participants of the Buck Creek REU program (Peterson et al., 2009) (Figure 2b). Oriented samples that preserve significant pristine olivine with minimum secondary hydration or alteration were collected across the Buck Creek ultramafic complex. Seven samples are from the Corundum Knob area, with three other samples from the eastern part of the body (Figure 2b). Lithologically, eight samples are dunites (NC13-9b, NC13-10, NC16-3, NC16-5, NC16-6a, NC16-12, NC16-13, and NC16-17). Sample NC16-6a is from an outcrop with thin dunite-troctolite cumulate layers, and NC16-2 is a meta-troctolite with olivine, plagioclase and a metamorphic symplectite. Sample numbers include a prefix indicating general location and sample year; in the rest of the paper, we reference only the sample numbers without prefix. International Geo Sample Numbers (IGSNs) are linked in Text S1.

The dominant planar fabric within the Buck Creek complex relates to the regional S2 foliation (Figure 2b). S2 is defined locally by weak flattening of olivine and plagioclase grains in dunite and troctolite and alignment of hydrous minerals, mainly amphiboles and chlorite. The Buck Creek body and S2 fabrics are folded at the map scale by upright, moderately NE-plunging regional F3 folds (Peterson et al., 2009). Hydrous secondary minerals locally define axial planar fabrics and intersection lineations associated with F3 folds. The granular nature of the olivine in these samples made it difficult to visually estimate olivine-defined planar and linear elements to confidently estimate SPO (X-Y-Z axes) for the olivine at the field or hand-sample scale. Thin sections were cut in our best estimate of the inferred X-Z plane (i.e., parallel to lineation and perpendicular to foliation). It is unclear how the strain reference frame that corresponds to olivine internal deformation relates to structural fabrics in surrounding rocks or those defined by secondary hydration minerals. The challenges with the determination of olivine SPO led us to alternative approaches (discussed below) to better define the strain reference frame appropriate for CPO interpretation.

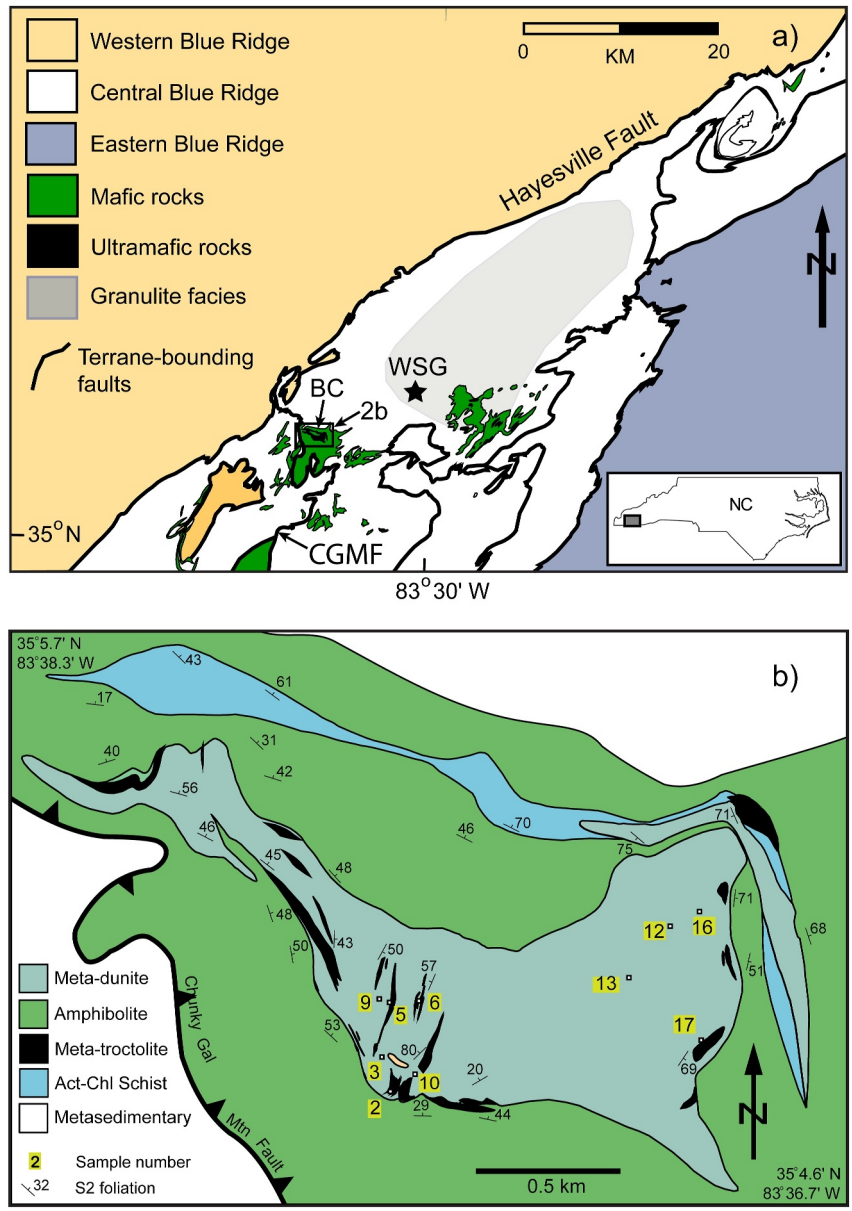

Figure 2. Location maps adapted from Peterson et al. (2009). (a) Tectonic setting of Buck Creek complex showing major Blue Ridge Terranes and terrane-bounding faults with North Carolina location map inset. BC = Buck Creek ultramafic complex (black) surrounded by Chunky Gal Mafic complex (green); CGMF = Chunky Gal Mountain Fault; WSG = Winding Stair Gap. Rectangle inset shows the location of (b). (b) Geologic map of Buck creek complex with sample locations.

2.2. Thin Section Textures

Olivine textures were described in plane- (PPL) and cross-polarized light (XPL) using the petrographic microscope facilities at Grand Valley State University. Textural observations were enhanced by high-resolution whole-section XPL photos of each sample. Observations included olivine grain shapes, size variation, grain boundary characteristics, and internal deformation features (e.g., undulose extinction or subgrain boundaries).

2.3. EBSD Analysis

Crystallographic orientations were determined via Electron Backscatter Diffraction (EBSD) at Washington and Lee University. Mechanically polished thin sections were subjected to a final polishing step using a 0.04 μm

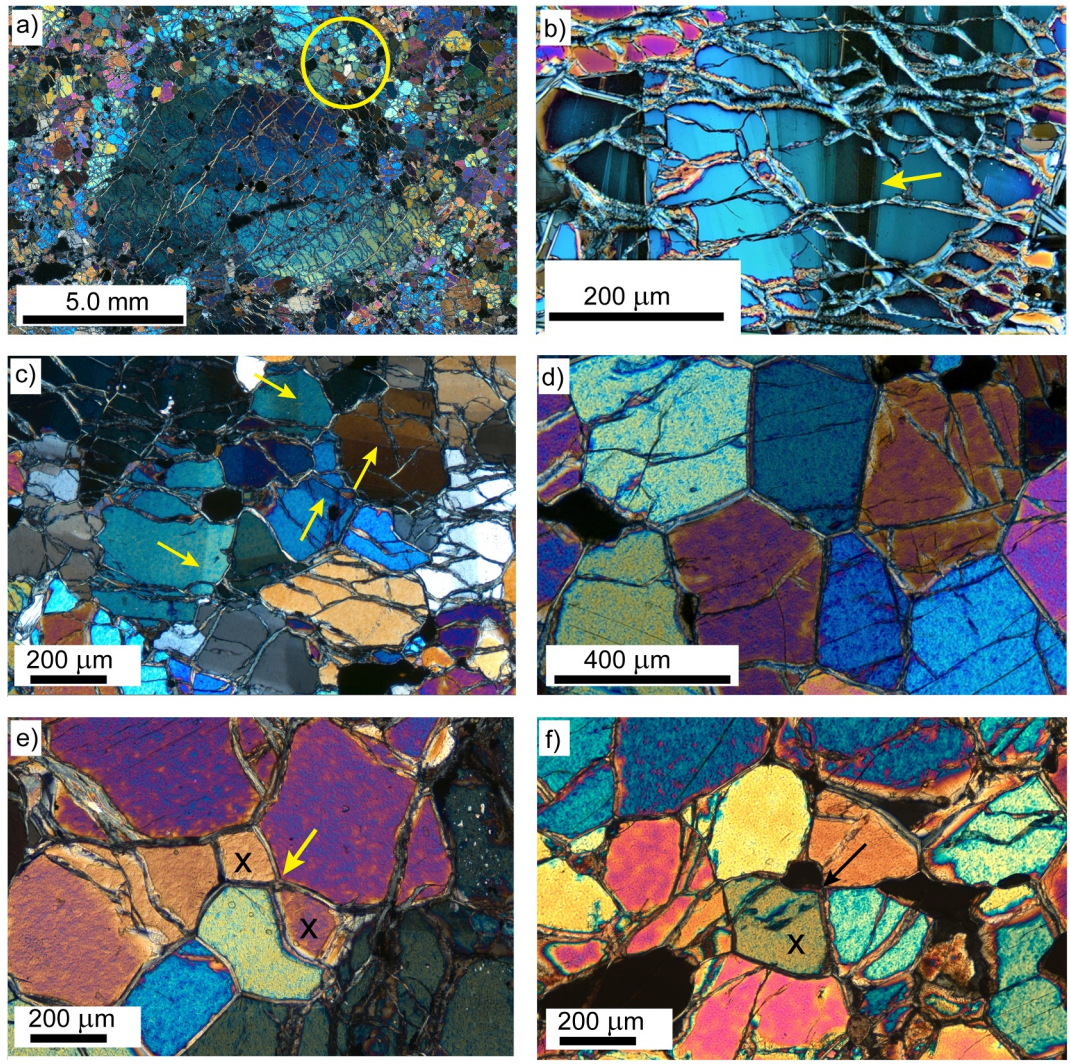

Figure 3. Thin section photomicrographs illustrating common textures. (a) Core and mantle structure with large relict olivine grain in center, exhibiting undulose extinction and surrounded by smaller recrystallized grains (e.g., circled area) (sample 3). (b) Kink banding within relict olivine grain (yellow arrow) cut by serpentine veins (sample 10). (c) Kink banding in ~orthogonal orientations (yellow arrows) within relict olivine grains (sample 5). (d) Annealed olivine grains with 120° triple junctions (sample 6a). (e) Diamond-shaped grains (x) intersecting at 4-grain junction (yellow arrow) (sample 5). (f) 4-grain junction (black arrow) and diamond-shaped grain (x) (sample 6a).

colloidal silica slurry. Data were acquired using a Zeiss EVO MA 15 Scanning Electron Microscope (SEM) using an Oxford Instruments Nordlys Nanodetector and AZtec software. Operating conditions included an accelerating voltage of 25 kV, a beam current of 20 nA, a working distance of ~25 mm, and a chamber pressure of 30 Pa. Given the size of the olivine grains (often >100 µm), large areas (typically 300–500 µm^2) were scanned to obtain representative textures. Scans were collected in 400 µm × 300 µm tiles, using a rectangular grid with an 8 µm step size that were merged into a single data set in AZtec and processed using the MTEX open source toolbox v. 5.8.1 (Bachmann et al., 2010). Low quality data (with mean angular deviation values >1.25°) and small grains (fewer than six pixels) included within larger olivine grains were interpreted to be spurious and filtered out of the data set. Large un-indexed areas with equant shapes (with a relatively low perimeter to area ratio) are treated as "grains" of non-indexed pixels; these regions are interpreted to represent secondary phases. Un-indexed areas with a large perimeter to area, such as fractures commonly observed in thin section (Figure 3), were removed from the data set to allow these olivine segments to be merged together. Grains were defined using a 15° misorientation between adjacent pixels and pole figures were plotted using one point per grain. Aspects of fabric texture were assessed quantitatively and calculated with routines presented in Mainprice et al. (2014). Investigated metrics include the

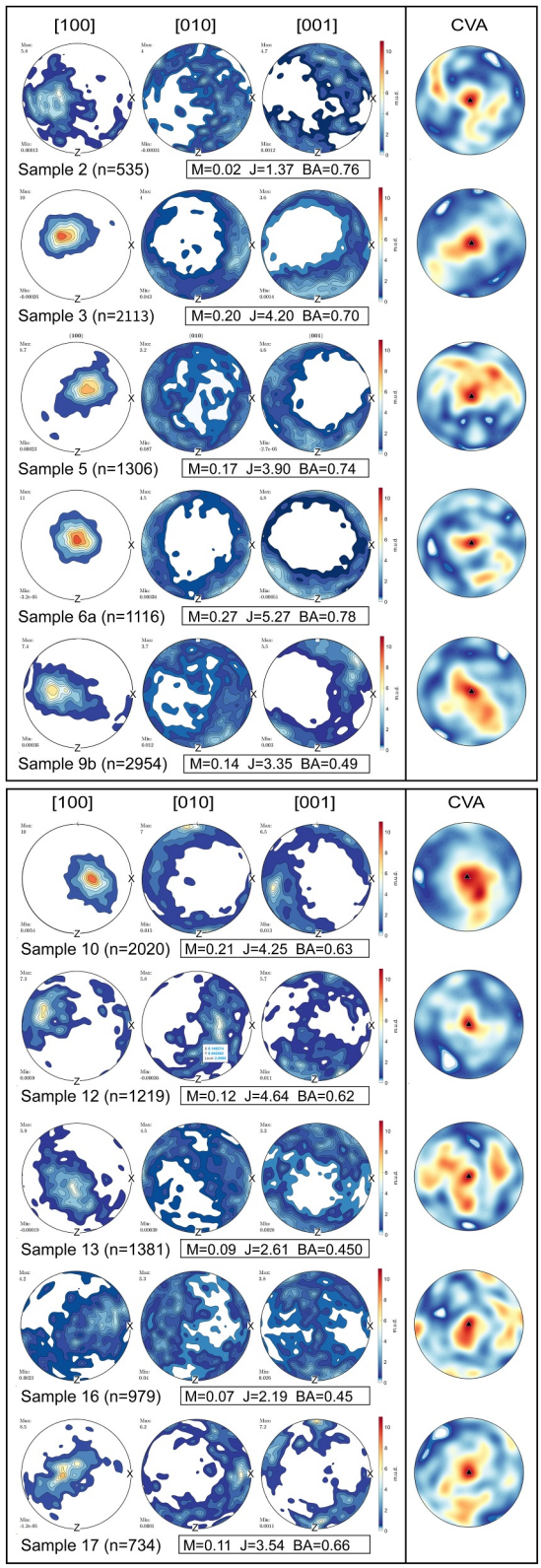

Figure 4.

M-index and J-index (which describe fabric strength) as well as Woodcock's (1977) K characteristic ($K > 1$ for point maxima and $K < 1$ for girdles) and the BA index (a measure of axial symmetry with BA = 0 related to axial-[010] and BA = 1 related to axial-[100]).

Olivine CPO fabrics are typically interpreted in a reference frame defined by the finite strain axes, with the Y-direction of strain at the center of a lower hemisphere stereonet and the X- and Z directions oriented E-W and N-S, respectively. We faced the common challenge (Cao et al., 2017; Chatzaras et al., 2016) of accurately recognizing the strain reference frame using macro-scale SPO in dunites with granular olivine and a locally developed secondary foliation defined by hydrous minerals. Despite our best efforts, our initial pole figure plots (Figure S1 in Supporting Information S1) revealed well-defined CPOs but with varied and unusual orientation patterns that suggest that our initial estimates of the X-Y-Z of strain reference frame were incorrect. We subsequently applied the methods described below to better approximate the appropriate reference frame for CPO interpretation.

2.4. Methods for Estimating Shape Fabrics

2.4.1. Crystallographic Vorticity Axis Approach

We assessed the SPO of our samples using crystallographic vorticity axis (CVA) analysis (Michels et al., 2015). In this method, the dispersion of crystallographic orientations from within individual grains is used to define a grain-scale vorticity axis, and the distribution of these axes from multiple grains provides an estimate of a sample-scale vorticity axis. Except in cases of transpressional deformation, the CVA axis will be parallel to the Y direction of finite strain. With an assumption of simple shear deformation (not transpression), this approach provides valuable information for orienting the EBSD data in a strain reference frame.

Although Michels et al. (2015) recommend a cut-off value of grain orientation spreads (GOS) > 1.0°, we observed that machine drift produced a small but systematic misorientation in weakly deformed grains that caused the inferred CVA axis to be consistently and erroneously placed in the same position for all samples. Thus, we restricted CVA analyses to grains with GOS > 2.0° (Figure S1 in Supporting Information S1). We rotated each data set to align the CVA with the Y-axis of the pole figure (center of the plot—Figure 4 CVA plots), though we note this approach provides no control on the orientation of the X or Z axes, which are oriented arbitrarily.

2.4.2. Olivine and Spinel Shape Fabric Analysis

Other studies have used spinel SPO determined with X-ray tomography to provide the strain reference frame for olivine pole figures (Cao et al., 2017; Chatzaras et al., 2016). We applied a similar reference frame approach using three mutually orthogonal thin sections (Van Ess & Peterson, 2018) to estimate

Figure 4. Contoured lower hemisphere equal area projections of olivine crystallographic axis orientations for each sample (CPO plots) representing one point per grain with n = #grains. Plots show M-, J-, and BA-indices for each sample. The contouring half-width is 10°. The X-Y-Z reference frames are based on reorientation from the original plots in Figure S1 in Supporting Information S1 using the CVA method described in the text. The right-hand plots show the contoured CVA data and selected CVA maxima rotated so that the maxima are at the center of the net and parallel to Y.

both the spinel and olivine SPOs. For three samples (3, 5, and 10), 2-D ellipses were fitted to olivine and spinel (chromite) grains (Text S1 in Supporting Information S1) and the SPO relative to the thin section was determined in the EllipseFit program (Vollmer, 2018); these were combined in the EllipseFit program to create a best-fit strain ellipsoid, taken to define the orientation of the 3-D X-Y-Z strain reference frame. We rotated the crystallographic data in MATLAB for each sample into these reference frames.

2.5. Assessment of Slip Systems

We assessed the slip systems active during olivine deformation using misorientation axes across subgrain boundaries. Dislocation motion can produce crystal domains separated by subgrain walls, with orientations related by a misorientation axis that is perpendicular to the direction of motion and within the slip plane (Chatzaras et al., 2016; Lloyd et al., 1997). For each sample, the inverse pole figures show misorientation axes associated with these boundaries that can be linked to active slip systems during olivine deformation. For an independent constraint, we spot-checked the slip systems for several samples using the Weighted Burgers Vector (Wheeler et al., 2024; Wieser et al., 2020).

2.6. Recrystallized Grain Size Piezometry Analysis

Paleopiezometry is founded in experimental work that demonstrates an inverse relationship between recrystallized grain size and differential stress. Karato et al. (1980) determined a piezometer equation based on experimental work on dry single-crystal olivine grains, while Van der Wal et al. (1993) developed an experimental calibration using "wet" natural dunites and "dry" data from Karato et al. (1980) that established a stress-recrystallized grain size relationship independent of temperature and water content.

Piezometer equations are written in the form $D_g = A\sigma^{-n}$ in which D_g is recrystallized grain size (μm), σ is differential stress (MPa), and A and n are empirically derived constants. We use the equation of Van der Wal et al. (1993) (Equation 1) to estimate differential stress from the size of dynamically recrystallized olivine grains in our samples.

$$D_g = 15000 * \sigma^{-1.33} \quad (1)$$

Thin sections were used for initial measurement of recrystallized grain size. We observed both larger grains, assumed to be relict, and smaller, equant grains with minimal internal deformation interpreted as recrystallized grains. For each thin section, the diameters of one hundred recrystallized grains with little or no internal deformation were measured in XPL along traverse lines.

We additionally estimated recrystallized grain size from EBSD data by adapting the method of Cross et al. (2017) developed for quartz (Figure S2 in Supporting Information S1). The revised code for olivine (Mennenga, 2024) is referenced in the Open Research section. This method evaluates intracrystalline lattice distortion to separate relict versus recrystallized grains by calculating the GOS values for each grain to identify recrystallized grains with low internal distortions. The EBSD method is effective for the identification of recrystallized grains and evaluates a larger sample size than the optical microscopy approach. Samples 3, 5, 6a, 9b, 10, 13, and 16 were dominated by well indexed olivine (Figure S2 in Supporting Information S1) that could be effectively used to estimate recrystallized grain size without effects of grain pinning by other primary or secondary minerals. The quality of indexing is spatially variable in sample 10; for it, we limit our piezometry analysis to a well-indexed subset of the full data set (about half of the full map; box in Figure S2 in Supporting Information S1). Three samples (2, 12, and 17) were not used for piezometry. Sample 2, dominated by plagioclase and symplectite, has minimal and widely spaced olivine. Samples 12 and 17 are altered by secondary minerals, leading to spaced and relatively poorly indexed olivine (Figure S2 in Supporting Information S1).

3. Results

3.1. Thin Section Textures

The dunite samples included larger relict olivine grains (~0.8–10 mm) interspersed with smaller (<0.5 mm) more equant recrystallized grains. Locally, we observed relict and recrystallized grains with core and mantle textures (Figure 3a). The relict grains are typically slightly elongate (up to ~2.5:1 length/width ratio) and preserve internal

deformation in the form of undulose extinction, subgrains, and kink boundaries (Figures 3a–3c). Bulging is less common and mostly evident from encapsulated grains and serrated boundaries along the relict grains (Figure 3a). Recrystallized grains show minor or no internal deformation and may display 120° grain boundaries, typical of annealing (Figure 3d). In places, we observed diamond-shaped grains with conjugate boundaries and grains intersecting in a 4-grain junction with ∼90° angles (Figures 3e and 3f).

Many samples include thin (∼10–30 μm) non-parallel serpentine-filled fractures that follow grain boundaries or cut across larger grains. The two troctolite samples contain plagioclase, separated from the olivine by a symplectite reaction texture (e.g., Tenthorey et al., 1996) and locally replaced by minor amphibole and mica. Euhedral to subhedral grains of chromium spinel are dispersed throughout each sample. Scattered thin grains of secondary chlorite cut across olivine grains, particularly in sample 16 as well as samples 2, 6a, 12, and 17.

3.2. EBSD Analysis

Seven of the eight dunite samples analyzed using EBSD (3, 5, 6a, 9b, 10, 13, and 16) are dominated by olivine with large numbers (>100,000) of well-indexed olivine analyses (Figure S1 in Supporting Information S1). Patchy poorly resolved areas in sample 12, extensive areas of plagioclase and symplectite in sample 2, and secondary chlorite in sample 17 resulted in fewer indexed olivine analyses (<100,000).

3.2.1. Crystallographic Preferred Orientation (CPO) Data

Plots of crystallographic data on lower hemisphere stereonets in our field-estimated strain reference frame (Figure S1 in Supporting Information S1) display [100] clustering with strongly to moderately defined maxima and more dispersed girdle patterns with moderate to poorly defined maxima for [010] and [001] axes. M-index values, indicating fabric strength, range from 0.016 to 0.271 (Table 1). The BA-index values, representing axial symmetry, range from 0.450 to 0.783, with most values above 0.60 (Table 1). For most samples, the K characteristics for [100] are >1 (point maxima) and those for [010] and [001] are <1 (girdles) (Table 1). The variable CPO patterns and the occurrence of CPOs with maxima not aligned with our inferred X-Y-Z directions suggest a reference frame issue that led us to attempt approaches to better identify the kinematically significant reference frame.

The X-Y-Z strain reference frame for the olivine CPO patterns does not appear to be influenced by local or regional structures. When reoriented to nets in a geographic reference frame, the orientations of [100] point maxima vary across the body in a pattern that is generally consistent with deformation by regional D2 and D3 fold structures. We also do not see evidence that shearing deformation associated with the Chunky Gal Mountain fault influences deformation features in our samples. The fault deformation features are primarily localized shear zones near the boundary between the amphibolite surrounding the dunite and the country rock with no related shear zones within the dunite body.

Reorientation of the CPO data using CVA analysis produced more consistent patterns for the [100] orientations (Figure 4). Six samples with well-indexed olivine and coherent EBSD grain maps (3, 5, 6a, 9b, 10, and 13) generate CPO patterns with a strong [100] maxima near the inferred vorticity axis/Y kinematic axis at the net center, and [010] and [001] girdles dispersed along the stereonet margins (Figure 4). Despite a well-indexed data set for sample 16, [100] orientations are generally clustered near the net center, but with a poorly defined maxima. The lower percentage of indexed olivine in samples 2, 12, and 17 (Figure S2 in Supporting Information S1) results in more dispersed CPO data. Similar to the other samples they display [100] clusters near the net center and [010] and [001] girdles, with the exception that the [100] cluster for sample 12 is closer to the net margin (Figure 4). These clusters are supported by our exploratory Weighted Burgers Vector analysis. We consistently find Weighted Burgers Vectors oriented parallel to [001] and at a high angle to both the trace of subgrain boundaries and the [100] direction (see Figure S3 in Supporting Information S1 for representative examples). These relationships suggest [001](010) slip, which produces clusters of [100] parallel to the kinematic Y direction, consistent with the reference frame determined by the CVA approach.

Our reorientation of the CPO data using olivine and spinel SPO from three samples with orthogonal thin sections produced mixed results (Figure 5). Reorientation of sample 3 data using both the olivine and spinel SPO reference frames results in [100] maxima near the Z-axis and girdle patterns across the center of the CPO plots for both [010] and [001] orientations (Figures 5a and 5b). Reorientation of sample 5 data into both the olivine and spinel

Table 1
Fabric Strength, Grain Size, and Stress Data From Buck Creek Samples

Sample	2[a,b]	3	5	6a	9b	10	12[b]	13[a]	16	17[b]
Indexing % of olivine versus non-indexed										
Raw indexing %	18	69	75	66	66	58	54	70	72	32
Indexing % after data cleaning	8.1	78.1	91.7	71.8	78.6	61.5	38.4	75.6	91.1	14.0
Fabric strength indices										
J factor	1.37	4.20	3.90	5.27	4.64	2.19	3.54	3.35	4.25	2.61
M index	0.016	0.199	0.169	0.271	0.125	0.065	0.110	0.144	0.209	0.087
BA	0.76	0.70	0.74	0.78	0.62	0.45	0.66	0.49	0.63	0.45
K [100]	4.97	1.59	2.26	6.91	0.74	2.44	5.46	0.69	1.11	0.55
K [010]	0.60	0.52	0.49	0.52	1.39	1.01	1.44	1.38	2.07	0.12
K [001]	0.54	0.66	0.27	0.41	1.49	1.40	6.77	1.89	1.91	2.08
Recrystallized grain size and piezometry										
EBSD Total Grains (#)	–	2208	1391	1128	2476	2028	–	1445	966	–
EBSD Relict Grains (#)	–	354	191	164	342	257	–	199	89	–
EBSD Rex Grains (#)	–	1854	1200	964	2134	1771	–	1246	877	–
%[c] Rex/Total Grains	–	84%	86%	85%	86%	87%	–	86%	91%	–
EBSD Arithmetic mean Rex (μm)	–	278.8	432.3	316.5	301.8	280.8	–	318.7	482.5	–
EBSD Geometric mean (μm)	–	234.7	339.1	272.4	231.5	228.3	–	234.6	358.5	–
EBSD Median Rex (μm)	–	224.4	335.4	277.6	228.4	203.9	–	223.6	355.9	–
EBSD RMS diameter (μm)	–	332.8	535.5	363.9	381.8	349.9	–	416.6	620.4	–
EBSD 2SD of mean (μm)	–	8.4	18.3	11.6	10.1	9.9	–	15.2	26.4	–
TS Rex grains mean (μm)[d]	–	166.03	142.90	140.07	162.41	114.99	130.94	–	133.15	127.07
TS Rex grains 2SD of mean (μm)[d]	–	21.14	23.11	14.99	17.98	17.30	12.38	–	15.96	14.86
TS Rex grains median (μm)[d]	–	138.96	109.18	124.07	151.36	96.77	126.55	–	114.14	124.07
VdW Stress (EBSD Median) (MPa)[e]	–	23.6	17.4	20.1	23.3	25.3	–	23.6	16.7	–
VdW Stress (TS Median) (MPa)[e]	–	17.5	12.3	16.4	15.8	16.9	36.3	14.8	11.0	36.8

[a]Recrystallized grain size was not calculated for TS samples 2 and 13. [b]Recrystallized grain size was not calculated using EBSD samples 2, 12, and 17. [c]Rex = recrystallized grains. [d]Thin section grain diameters out of 100 measured grains. [e]Van der Wal et al. (1993) piezometer using median grain size.

SPO reference frames results in [100] maxima near the center of the CPO plots, although the [100] maxima in the spinel SPO reference frame lies ~halfway between the center (Y) and the X-direction (Figures 5c and 5d). The [010] and [001] orientations in the CPO plots for both olivine and spinel reference frames are dispersed around the outside of the net with no clear maxima. Reorientation of sample 10 data into both the olivine and spinel SPO reference frames results in CPO plots that differ from each other. Within the olivine SPO reference, the [100] maxima lie near Z, [010] near Y and [001] near X (Figure 5e). Within the spinel SPO reference frame, the [100] maxima lie near Y, [010] near X and [001] near Z (Figure 5e).

3.2.2. Misorientation Data

The inverse pole figures (Figure 6) display the misorientation axes, defined by misorientation angles >5°, across subgrain boundaries in a crystallographic reference frame that reflects the specific active slip systems. Typical misorientation directions associated with tilt walls are shown in Figure 6 inset, while misorientation around twist walls is at 90° from the tilt wall orientations. Most samples in this study have misorientation clusters at or near [100] on the inverse pole figures (Figure 6). Sample 3 has a cluster at [010] with spread toward [100], and sample 9b has orientations slightly offset from [100] in the direction of [010].

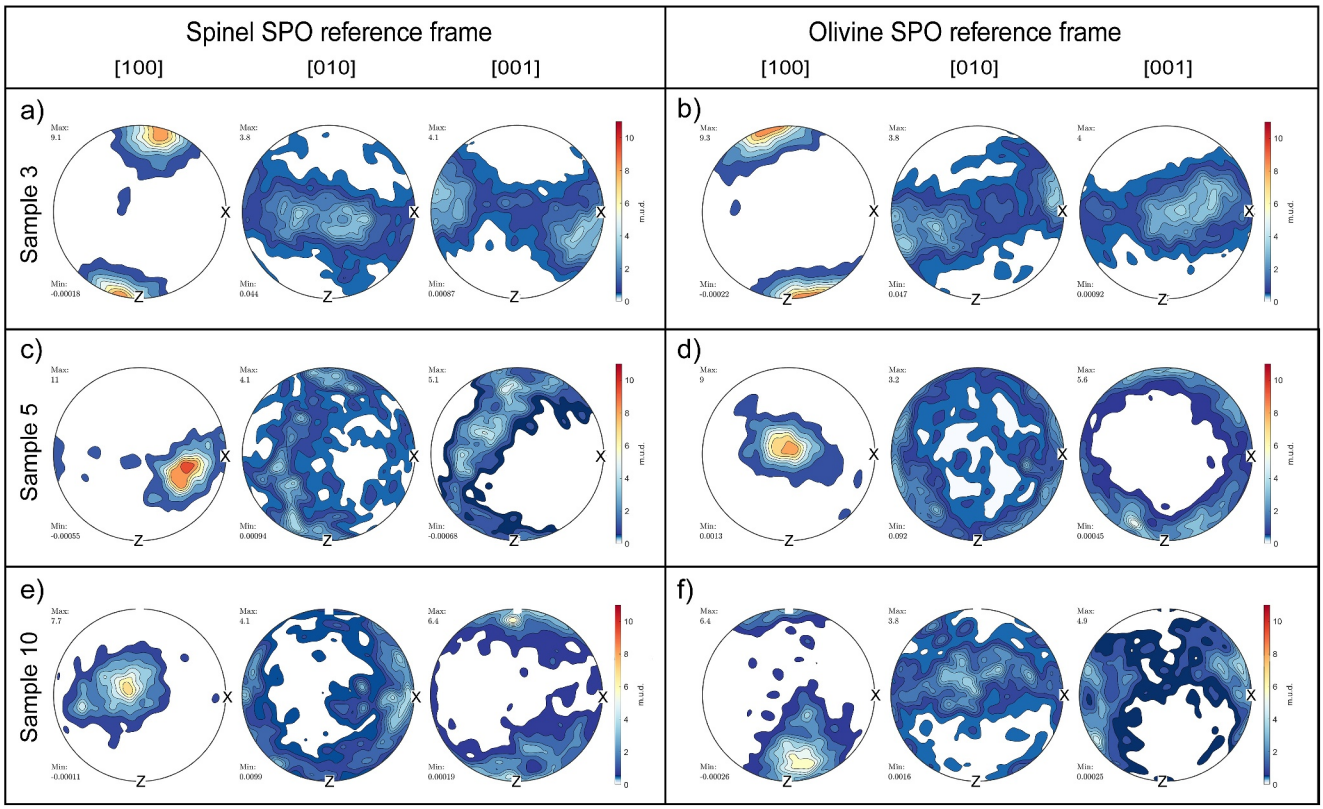

Figure 5. Contoured lower hemisphere equal area projections of olivine CPO for samples 3, 5, and 10. The data shown in these plots was reoriented from the original plots in Figure S1 in Supporting Information S1 into a strain reference frame determined from the SPO ellipsoids for spinel (left side) and olivine (right side) determined using three orthogonal thin sections as described in the text.

3.2.3. Recrystallized Grain Size and Differential Stress Analysis

Relict and recrystallized grains from samples and sample domains with well indexed olivine and minimal interference from other minerals (Samples 3, 5, 6a, 9b, part of 10, 13, and 16) were identified using our EBSD data and the method of Cross et al. (2017), with results reported in Table 1 and the resulting maps and histograms of the relict and recrystallized grains in Figure S2 in Supporting Information S1. In the samples we did not use for piezometry, the maps are dominated by large non-indexed areas with dispersed tiny grains that may reflect grains that experienced secondary alteration or pinning by adjacent grains. These tiny grains overestimate the stress. Overall, 84%–91% of grains are recrystallized, with median recrystallized grain sizes ranging from 204 to 356 μm. The maps (Figure S2a in Supporting Information S1) illustrate that relict grains generally appear larger and less equant than recrystallized grains. The histograms (Figure S2 in Supporting Information S1) document that a significant population of small relict grains overlap in size with recrystallized grains. This might be explained by the early formation of recrystallized grains that later accumulated additional strain (Cross et al., 2017). Recrystallized grain size is significantly skewed toward larger grains (Figure S2b in Supporting Information S1), so median values (similar to the geometric mean—Table 1) represent the recrystallized grain population better than the arithmetic mean or RMS diameter and are used for piezometry.

The differential stress estimates for the Buck Creek samples using median recrystallized grain size from the EBSD method and the Van der Wal et al. (1993) piezometer (Table 1) range from 17 to 25 MPa with an average of ~22 MPa. Average stress estimates using thin section data are ~2 MPa higher (Table 1). There is no evident pattern related to geography or sample characteristics that explains the variation in stress and grain size values among the samples.

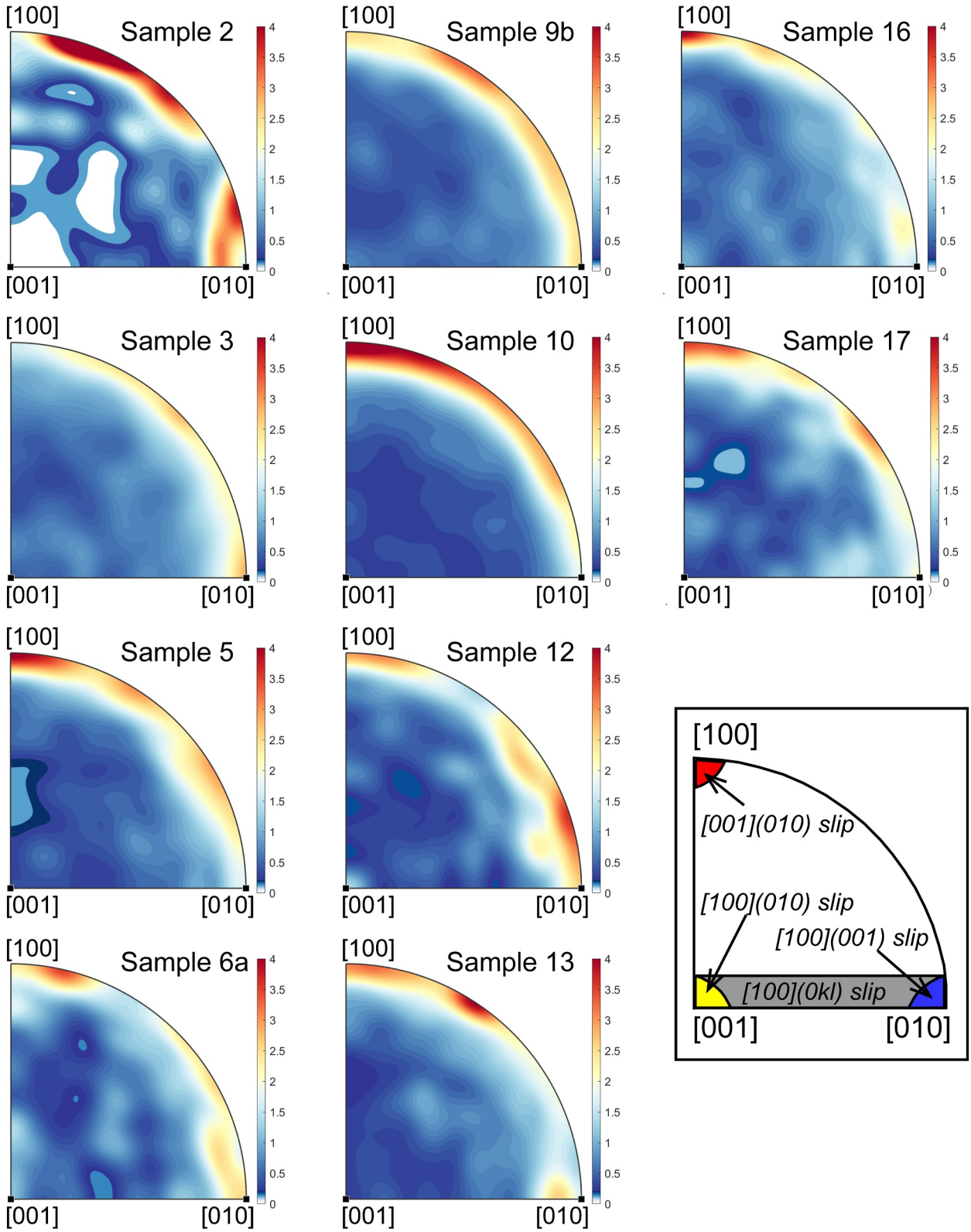

Figure 6. Inverse pole plots showing misorientation axes for each sample. Inset shows typical clustering for common slip system types with subgrain formation by tilt walls, after de Kloe et al. (2002) and Chatzaras et al. (2016). A-type fabrics with [100](010) slip cluster near the [001] corner (yellow shading). B-type fabrics with [001](010) slip cluster near [100] (red shading). C-type fabrics with [100] (001) slip cluster near [100] (blue shading).

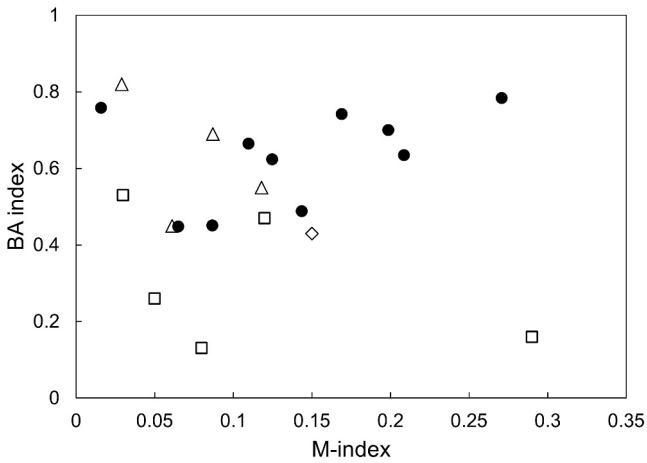

Figure 7. M-index versus BA-index data comparing Buck Creek samples (solid circles) to published naturally occurring B-type samples (open symbols). Bernard et al. (2019) (open square); Cao et al. (2017) (open triangles); Chatzaras et al. (2016) (open diamond).

4. Discussion

4.1. Evidence for Dominance of B-Type Olivine Deformation

Most of our new crystallographic data show that olivine fabrics from the Buck Creek complex are of the B-type with well-developed CPO maxima and moderate fabric strengths (J-indices from 1.37 to 5.27; M-indices from 0.016 to 0.271) (Table 1). Misorientation axes for almost all samples cluster strongly near [100] (Figure 6a), a pattern produced by the [001](010) slip system (Figure 6b) characteristic of B-type deformation fabrics (Chatzaras et al., 2016; de Kloe et al., 2002). In contrast, sample 3 has its strongest clustering near [010], interpreted to result from [001](100) slip typical of C- or E-type fabrics (Chatzaras et al., 2016; de Kloe et al., 2002). Sample 9b has a maximum between [100] and [010] that could be explained by the activity of both B-type [001](010) and C- or E-type [001](100) slip systems or by dominantly B-type fabrics with both tilt and twist activity to build subgrain boundaries (de Kloe et al., 2002).

For most samples, rotating our CPO data using the CVA method (Figure 4) produces well-defined maxima of [100] near the center (Y-axis) of each stereonet, uniquely indicative of B-type fabrics. This result holds despite the inability of this approach to provide the orientation of the X and Z axes. Our alternative approach to reorient the CPO data into the estimated olivine and spinel 3D SPO reference frames for samples 3, 5, and 10 generated mixed results (Figure 5). For sample 5, both olivine and spinel reorientations generate a pattern consistent with B-type patterns from both CVA analysis and misorientation axis data. However, reorientation of sample 3 in both olivine and spinel SPO reference frames (Figures 5a and 5b) produces CPO patterns more typical of C-type fabrics. Although this is different from the B-type patterns suggested by CVA analysis (Figure 4), it is consistent with the misorientation data clustering near [010] for sample 3, a pattern common for C-type fabrics (Figure 6b). Sample 10 data, reoriented in the olivine SPO reference frame, also produce a C-type fabric, but the spinel SPO and CVA plots and misorientation data are more consistent with the B-type.

The girdle patterns defined by the [010] and [001] orientations in our data are distinct from point clusters typical of experimentally determined B-type patterns, instead showing fiber-type CPO patterns similar to axial-type patterns. Our samples with point clusters for all crystallographic axes have BA close to 0.5. Most of the Buck Creek samples have [010] and [001] girdles linked to $K < 1$ and sample BA values > 0.60 (Figure 7). BA indices for three of the natural B-type samples from Cao et al. (2017) (Figure 7) show a similar range to those for Buck Creek and also display [010] and [001] girdle patterns. Other published natural B-type samples (Bernard et al., 2019; Chatzaras et al., 2016) have BA index values near or below 0.5 (Figure 7). Although our CPO data and misorientation axis distributions are not consistent with D-type deformation, the proposed explanations for the girdling patterns associated with D-type fabrics are instructive. These include competition between slip systems (Hansen et al., 2014), higher strain conditions (Hansen et al., 2014), the activity of dislocation accommodated grain boundary sliding (DisGBS) that facilitates the operation of two slip systems (Warren et al., 2008), and the influence of a pre-existing texture (Boneh & Skemer, 2014). We do not have convincing evidence that points to one of these factors influencing the development of the [010][001] girdle patterns. Perhaps evidence of [001](100) slip (C-type fabrics) could point to competition between the two slip systems. The presence of textures associated with both dislocation glide and GBS could suggest the activity of more than one deformation mechanism.

On the whole, our crystallographic data support the dominant activity of the [001](010) slip system and formation of B-type fabrics associated with deformation for most of the Buck Creek dunite samples, with some evidence from misorientation analysis for sample 3 and SPO reorientation of samples 3 and 10 for [001](100) slip and the formation of C-type fabrics. Deformation conditions may have been near the B-C type boundary, such that these results reflect local variations in stress or temperature conditions or local preservation of earlier C-type fabrics formed at higher temperatures.

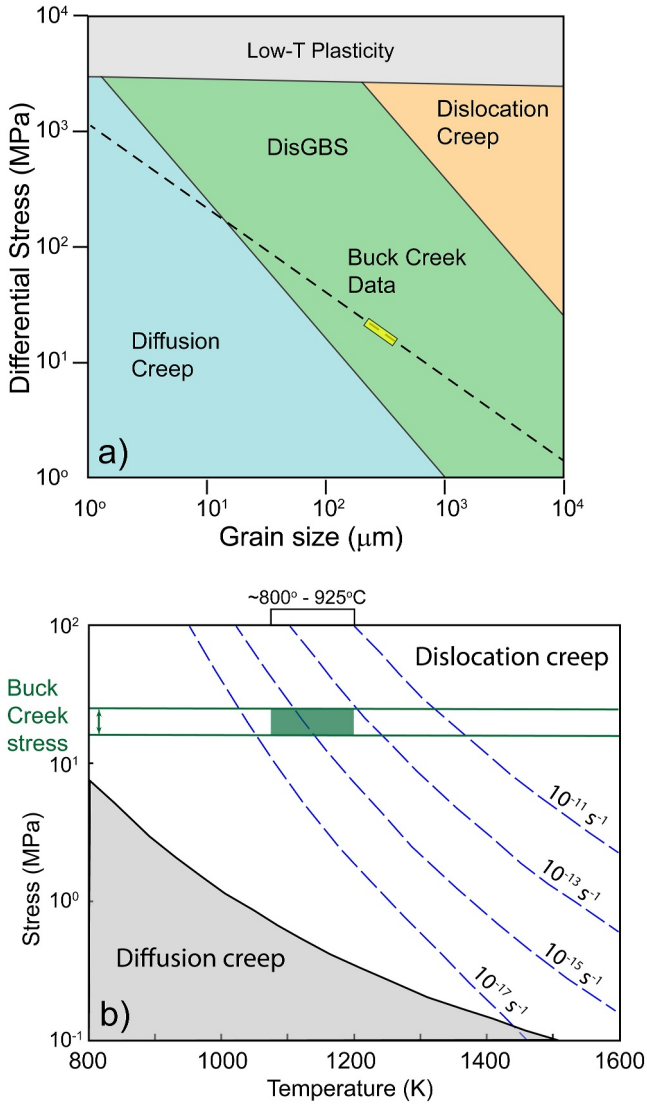

Figure 8. Comparison of Buck Creek conditions to deformation mechanisms. (a) Olivine deformation mechanism map for conditions of 850°C, 1400 MPa, adapted from Chatzaras et al. (2016) with Van der Wal et al. (1993) piezometer (dashed line) and range of Buck Creek median Grain size-Stress data (yellow rectangle). (b) Plot of Temperature versus Stress conditions adapted from Cao et al. (2015) for pressures of 1.5 GPa at dry conditions with strain rate contours showing the range of Buck creek temperature and stress conditions.

4.2. Differential Stress and Deformation Conditions for the Buck Creek Complex

Differential stress estimates for the Buck Creek olivine samples using piezometry (Van der Wal et al., 1993) indicate relatively low stress deformation conditions of 17–25 MPa (Table 1). Textures indicative of some annealing and growth of recrystallized grains suggest that these estimates represent lower bounds on stress. Peak metamorphic conditions for the Buck Creek body have been estimated at 825–850°C and 1.0–1.4 GPa (Emilio, 1998; Tenthorey et al., 1996). When plotted onto the deformation mechanism map calculated by Chatzaras et al. (2016) for conditions of 850°C and 1400 MPa (Figure 8a), our grain-size—stress data falls within the field of DisGBS (Figure 8a). On a temperature—stress deformation mechanism map (Figure 8b) adapted from Cao et al. (2015), calculated for dry conditions at 1.5 GPa, the Buck Creek olivine data plots within the field of dislocation creep within the range of natural strain rates (10^{-13}–10^{-15} s^{-1}). Textures observed in thin sections, such as undulose extinction, subgrains and kink band textures (Figures 3a–3c) are most consistent with dislocation creep. Fewer microstructures are consistent with grain boundary sliding (GBS), including 4-grain junctions and diamond shaped grains (Figures 3e and 3f).

The stress—temperature conditions estimated for the Buck Creek dunites (17–25 MPa and 825–850°C) are well within the range for B-type fabrics documented for natural samples by Bernard et al. (2019) and at the low temperature range of C-type fabrics (Figure 1b). Our samples also fall near the low-T and low-stress boundary between B- and C-type deformations extrapolated by Katayama and Karato (2006) from experimental data (Figure 1b). Peak metamorphic assemblages and textures in Buck Creek samples indicate that the rocks were not water saturated and in fact were relatively dry with evidence for a small amount of water available to form local amphibole-spinel symplectites (Lang et al., 2004; Tenthorey et al., 1996). These lower water contents are also consistent with the range of natural B-type fabrics documented by Bernard et al. (2019). In summary, the Buck Creek dunites appear to have been deformed by the activity of the [001] (010) slip system (B-type fabrics) at conditions of relatively low differential stress, low temperature, and low water content.

4.3. Tectonic Setting and Deformation Conditions Associated With B-Type Fabric at Buck Creek

The olivine-rich rocks preserved in the Buck Creek ultramafic complex have been interpreted to represent part of an ocean ridge cumulate complex that was partially subducted during the Taconic orogeny and emplaced into the base of the Laurentian continental crust (Peterson et al., 2009). Mineral assemblages and textures preserved in meta-troctolites within the Buck Creek complex are particularly useful in constraining the conditions during deformation of ~800°C, 1.0–1.4 GPa, with negligible fluid content (Lang et al., 2004; Tenthorey et al., 1996). Thus, we primarily consider two settings of formation for the B-type fabrics in the Buck Creek dunites: (a) they formed in a cumulate setting or (b) they developed contemporaneously with emplacement in the subduction wedge.

B-type fabrics that develop in a cumulate setting form during compaction of a crystal mush associated with melt-assisted GBS (Cao et al., 2017; Yao et al., 2019). Such fabrics are typically associated with high temperatures, low pressures, and low water contents due to the incompatibility of water in the fractionation system. B-type fabrics formed in this setting tend to have relatively weak SPO and CPO (m-index 0.05–0.13) (Yao et al., 2019). The Buck Creek dunites preserve weak olivine SPO and minor textural evidence of GBS, consistent with a cumulate setting. However, a strong CPO suggested by the clustering of the [100] crystallographic axes and m-indices

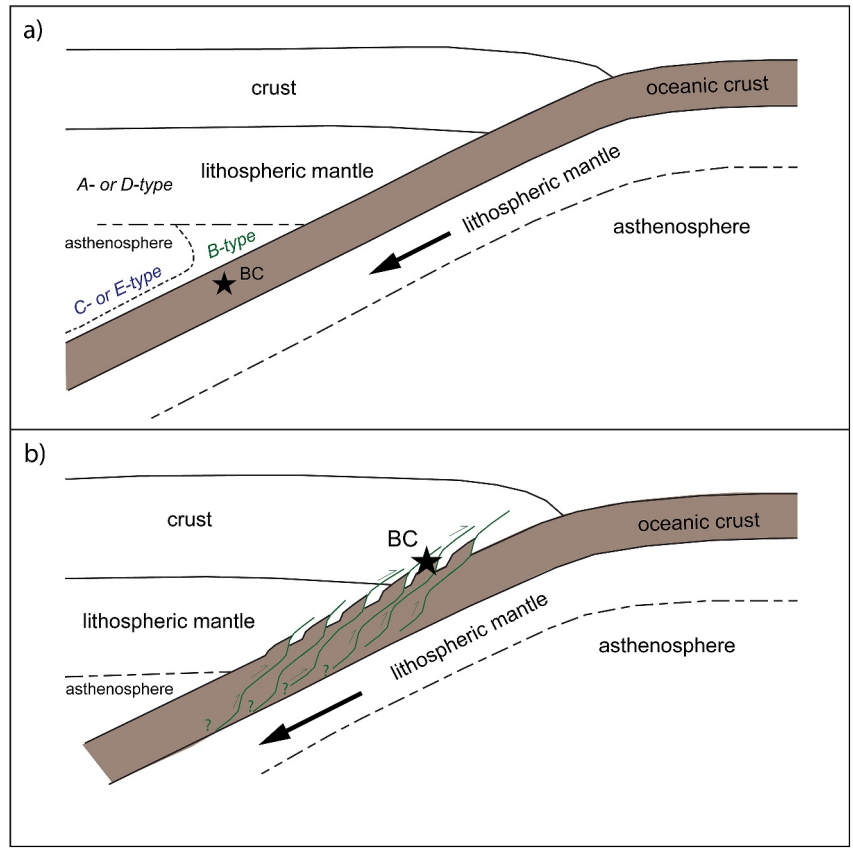

Figure 9. Schematic tectonic setting adapted from Cao et al. (2017) for mature cool subduction zones showing mantle wedge region of B-type and transition to C-type (dotted) and emplacement into upper plate. Sketches not to scale and thickness of oceanic crust are exaggerated. (a) Subduction setting showing regions of formation A, B, C type fabrics and possible setting of deformation of Buck Creek (BC—black star). (b) Illustration of possible emplacement process related to tectonic underplating of slices of oceanic crust including BC into overriding plate.

reaching as high as 0.27 as well as textural evidence for the dominance of dislocation creep suggest the Buck Creek B-type fabrics did not develop in the cumulate setting or by melt-enhanced GBS.

B-type olivine fabrics are commonly linked to formation in the cold upper mantle wedge in the vicinity of the subducting slab (Figure 9a). The activity of [001](010) slip systems associated with B-type fabrics aligns the seismically fast olivine *a* axis perpendicular to the stretching direction, helping explain the common trench-parallel S-wave polarization in the shallow wedge (e.g., Kneller et al., 2007). B-type fabrics in the shallow mantle wedge are generally associated with relatively low temperatures and high stress under water saturated conditions. Modeling by Kneller et al. (2005) indicates that the temperature and differential stress conditions associated with B-type fabrics (>700–800°C, 50–70 MPa) are favored in the shallow wedge. Within the wedge, the depth of transition to C-type fabrics increases with slower subduction rates and a deeper transition from partial to full coupling of the subducting slab (Kneller et al., 2005). B- and C-type fabrics from natural samples form at similar stress ranges below ~50 MPa (Bernard et al., 2019) and B-type fabrics are favored over C-type fabrics in samples deformed at lower temperatures under water saturated conditions (>200 ppm H/Si) (Bernard et al., 2019; Katayama & Karato, 2006). For natural samples in the upper mantle, olivine slip systems appear to be less sensitive to water and stress conditions than indicated by experimental work (Bernard et al., 2019), such that water saturation is less critical to the formation of B-type fabrics. The inferred tectonic emplacement of the Buck Creek complex as a fragment of subducting ocean crust into the lower Laurentian continental crust places the complex at conditions of deformation consistent with shallow mantle wedge formation of B-type fabrics (Figure 9a). The temperature and stress conditions estimated for Buck Creek are similar to other natural samples with B-type fabrics in this mantle wedge setting (Bernard et al., 2019), with the distinction of forming under nearly anhydrous conditions. We envision a model similar to the emplacement of mantle slices into the overlying crust in a

subduction setting as shown in Cao et al. (2015), though the Buck Creek dunites are interpreted to be slices of cumulate rock from the subducting ocean crust (Figure 9b). Notably, this means that the dunites experienced deformation conditions similar to those in the mantle wedge during subduction and emplacement, despite originating in the down-going oceanic crust. The hint of activity of C-type fabrics in samples 3 and 10 could indicate that the Buck Creek dunites deformed somewhere near the transition at depth in the mantle wedge from B- to C-type fabrics. The stress—temperature conditions for the Buck Creek samples fall near the B-C type transition (Figure 1b), suggesting the possibility the rocks reached depths and temperatures favorable to development of C-type fabrics.

Thus, we suggest that the main olivine fabrics in the Buck Creek samples formed during subduction; however, weak B-type fabrics may have formed early during cumulate formation within the ocean crust. The [010] and [001] girdle patterns in our data may reflect GBS activity or overprinting of pre-existing fabrics. As these ocean crust dunites were subducted beneath Laurentia, conditions favorable to the formation of B-type fabrics in the shallow mantle wedge were similar to those in the adjacent subducting slab (Figure 9a). Stress-temperature conditions for the Buck Creek samples lie near the transition from B- to C-type fabrics and hints of C-type patterns are consistent with the Buck Creek rocks reaching depth and temperature conditions near the B-C transition prior to emplacement into the overlying Laurentian continental crust (Figure 9b).

5. Conclusions

The olivine-rich rocks preserved in the Buck Creek ultramafic complex have been interpreted to originate as part of an ocean ridge cumulate complex that was partially subducted during the Taconic orogeny and emplaced into the base of the Laurentian continental crust (Peterson et al., 2009). The rocks preserve evidence of relatively dry conditions at peak metamorphic conditions of ∼800°C, 1.0–1.4 GPa, with localized hydration that possibly assisted emplacement. We present evidence that olivine is primarily deformed by [001](010) slip, generating B-type olivine fabrics at low differential stress of ∼17–25 MPa. We document that the conditions for formation of B-type fabrics at Buck Creek form at lower differential stress conditions and lower water content than typically reported, broadening the range of conditions of formation of B-type fabrics. Additionally, there is evidence of C-type fabrics caused by a fabric transition with depth. The Buck Creek olivine preserves evidence of deformation by dislocation creep, accommodated by grain boundary sliding as indicated by textures and the position of the samples on deformation mechanism maps.

We suggest that the Buck Creek dunites formed as ocean crust cumulates and were subducted beneath the Laurentian continental crust to depths of ∼30–40 km (Peterson et al., 2009) where the olivine experienced deformation conditions similar to conditions in the shallow mantle wedge to form B-type fabrics. Localized hydration at peak conditions may have facilitated the emplacement of the Buck Creek complex as a slice of subducting ocean crust (Peterson et al., 2009).

Data Availability Statement

The results of this work are included in the text's main figures, Table 1, and in Figures S1–S3 in Supporting Information S1 of the article. All Electron Backscatter Diffraction (EBSD) data used in this study are available online through the EarthChem Data Repository at Peterson et al. (2025). MATLAB code used to evaluate EBSD data was adapted from the MTEX Toolbox (Mainprice et al., 2014). MATLAB code adapted from Cross et al. (2017) for use with olivine data is available at Mennenga (2024).

Acknowledgments
This work was supported by a Michigan Space Grant Consortium Seed Grant 15-16 (to Peterson). In addition, Grand Valley State University and the Geology Department provided resources and support including the Norman and Helen Gibson Geology Field Study Scholarship (to Mennenga in 2020). We gratefully acknowledge John Wheeler for providing the Crystalscape software used for the Weighted Burgers Vector analysis and Andrew Cross and Katy Johanesen for their constructive and insightful reviews.

References

Bachmann, F., Hielscher, R., & Schaeben, H. (2010). Texture analysis with MTEX—Free and open source software toolbox. *Solid State Phenomena*, *160*, 63–68. https://doi.org/10.4028/www.scientific.net/SSP.160.63

Behr, W. M., & Smith, D. (2016). Deformation in the mantle wedge associated with Laramide flat-slab subduction. *Geochemistry, Geophysics, Geosystems*, *17*(7), 2643–2660. https://doi.org/10.1002/2016GC006361

Bernard, R. E., Behr, W. M., Becker, T. W., & Young, D. J. (2019). Relationships between olivine CPO and deformation parameters in naturally deformed rocks and implications for mantle seismic anisotropy. *Geochemistry, Geophysics, Geosystems*, *20*(7), 3469–3494. https://doi.org/10.1029/2019GC008289

Boneh, Y., & Skemer, P. (2014). The effect of deformation history on the evolution of olivine CPO. *Earth and Planetary Science Letters*, *406*, 213–222. https://doi.org/10.1016/j.epsl.2014.09.018

Cao, Y., Jung, H., & Song, S. (2017). Olivine fabrics and tectonic evolution of fore-arc mantles: A natural perspective from the Songshugou dunite and harzburgite in the Qinling orogenic belt, central China: Olivine fabric and fore-arc evolution. *Geochemistry, Geophysics, Geosystems*, *18*(3), 907–934. https://doi.org/10.1002/2016GC006614

Cao, Y., Jung, H., Song, S., Park, M., Jung, S., & Lee, J. (2015). Plastic deformation and seismic properties in fore-arc mantles: A petrofabric analysis of the Yushigou Harzburgites, North Qilian Suture Zone, NW China. *Journal of Petrology*, *56*(10), 1897–1944. https://doi.org/10.1093/petrology/egv053

Carter, N. L., & Ave'Lallemant, H. G. (1970). High temperature flow of dunite and peridotite. *Geological Society of America Bulletin*, *81*(8), 2181–2202. https://doi.org/10.1130/0016-7606(1970)81[2181:HTFODA]2.0.CO;2

Chatzaras, V., Kruckenberg, S. C., Cohen, S. M., Medaris, L. G., Withers, A. C., & Bagley, B. (2016). Axial-type olivine crystallographic preferred orientations: The effect of strain geometry on mantle texture: Strain geometry controls olivine texture. *Journal of Geophysical Research: Solid Earth*, *121*(7), 4895–4922. https://doi.org/10.1002/2015JB012628

Cross, A., Prior, D., Stipp, M., & Kidder, S. (2017). The recrystallized grain size piezometer for quartz: An EBSD-based calibration. *Geophysical Research Letters*, *44*(13), 6667–6674. https://doi.org/10.1002/2017GL073836

de Kloe, R., Drury, M., & Farrer, J. (2002). Determination of activated slip systems in experimentally deformed olivine-orthopyroxene polycrystals using EBSD. *Microscopy and Microanalysis*, *8*(S02), 680–681. https://doi.org/10.1017/S1431927602106404

Drury, M., Lallemant, H. A., Pennock, G., & Palasse, L. (2011). Crystal preferred orientation in peridotite ultramylonites deformed by grain size sensitive creep, Étang de Lers, Pyrenees, France. *Journal of Structural Geology*, *33*(12), 1776–1789. https://doi.org/10.1016/j.jsg.2011.10.002

El-Shazly, A. K., Loehn, C., & Tracy, R. J. (2011). P–T–t evolution of granulite facies metamorphism and partial melting in the Winding Stair Gap, Central Blue Ridge, North Carolina, USA. *Journal of Metamorphic Geology*, *29*(7), 753–780. https://doi.org/10.1111/j.1525-1314.2011.00940.x

Emilio, M. C. (1998). *Metamorphic evolution of the Buck Creek mafic-ultramafic complex, Clay County, North Carolina, USA [M.S.]*. University of South Florida.

Hadley, J. B. (1949). Preliminary report on corundum deposits in the Buck Creek peridotite, Clay County, North Carolina: U.S. *Geological Survey Bulletin*, *948-E*, 103–128. https://doi.org/10.3133/b948E

Hansen, L. N., Zhao, Y.-H., Zimmerman, M. E., & Kohlstedt, D. L. (2014). Protracted fabric evolution in olivine: Implications for the relationship among strain, crystallographic fabric, and seismic anisotropy. *Earth and Planetary Science Letters*, *387*, 157–168. https://doi.org/10.1016/j.epsl.2013.11.009

Hatcher, R. D. (1978). Tectonics of the western Piedmont and Blue Ridge, southern Appalachians; review and speculation. *American Journal of Science*, *278*(3), 276–304. https://doi.org/10.2475/ajs.278.3.276

Hibbard, J., Van Staal, C., Rankin, D., & Williams, H. (2006). *Lithotectonic map of the Appalachian Orogen, Canada-United States of America*. Bulletin of the Geological Survey of Canada. map 2096A(500). https://doi.org/10.4095/221912

Jung, H. (2009). Deformation fabrics of olivine in Val Malenco peridotite found in Italy and implications for the seismic anisotropy in the upper mantle. *Lithos*, *109*(3–4), 341–349. https://doi.org/10.1016/j.lithos.2008.06.007

Jung, H., Katayama, I., Jiang, Z., Hiraga, T., & Karato, S.-I. (2006). Effect of water and stress on the lattice-preferred orientation of olivine. *Tectonophysics*, *421*(1–2), 1–22. https://doi.org/10.1016/j.tecto.2006.02.011

Jung, H., Mo, W., & Choi, S. (2009). Deformation microstructures of olivine in peridotite from Spitsbergen, Svalbard and implications for seismic anisotropy. *Journal of Metamorphic Geology*, *27*(9), 707–720. https://doi.org/10.1111/j.1525-1314.2009.00838.x

Jung, H., Mo, W., & Green, H. W. (2009). Upper mantle seismic anisotropy resulting from pressure-induced slip transition in olivine. *Nature Geoscience*, *2*(1), 73–77. https://doi.org/10.1038/ngeo389

Jung, S., Jung, H., & Austrheim, H. (2014). Characterization of olivine fabrics and mylonite in the presence of fluid and implications for seismic anisotropy and shear localization. *Earth Planets and Space*, *66*, 1–21. https://doi.org/10.1186/1880-5981-66-46

Karato, S., Jung, H., Katayama, I., & Skemer, P. (2008). Geodynamic significance of seismic anisotropy of the upper mantle: New insights from laboratory studies. *Annual Review of Earth and Planetary Sciences*, *36*(1), 59–95. https://doi.org/10.1146/annurev.earth.36.031207.124120

Karato, S., Toriumi, M., & Fujii, T. (1980). Dynamic recrystallization of olivine single crystals during high-temperature creep. *Geophysical Research Letters*, *7*(9), 649–652. https://doi.org/10.1029/GL007i009p00649

Katayama, I., & Karato, S. (2006). Effect of temperature on the B-to C-type olivine fabric transition and implication for flow pattern in subduction zones. *Physics of the Earth and Planetary Interiors*, *157*(1–2), 33–45. https://doi.org/10.1016/j.pepi.2006.03.005

Kim, D., & Jung, H. (2015). Deformation microstructures of olivine and chlorite in chlorite peridotites from Almklovdalen in the Western Gneiss Region, southwest Norway, and implications for seismic anisotropy. *International Geology Review*, *57*(5–8), 650–668. https://doi.org/10.1080/00206814.2014.936054

Kneller, E., Van Keken, P., Katayama, I., & Karato, S.-I. (2007). Stress, strain, and B-type olivine fabric in the fore-arc mantle: Sensitivity tests using high-resolution steady-state subduction zone models. *Journal of Geophysical Research*, *112*(B4). https://doi.org/10.1029/2006JB004544

Kneller, E. A., Van Keken, P. E., Karato, S., & Park, J. (2005). B-type olivine fabric in the mantle wedge: Insights from high-resolution non-Newtonian subduction zone models. *Earth and Planetary Science Letters*, *237*(3–4), 781–797. https://doi.org/10.1016/j.epsl.2005.06.049

Kohlstedt, D. L., & Holtzman, B. K. (2009). Shearing melt out of the Earth: An experimentalist's perspective on the influence of deformation on melt extraction. *Annual Review of Earth and Planetary Sciences*, *37*(1), 561–593. https://doi.org/10.1146/annurev.earth.031208.100104

Lacazette, A. J., Jr., & Rast, N. (1989). Tectonic mélange at Chunky Gal Mountain, North Carolina. In *Mélanges Olistostromes of the U.S. Appalachians* (Vol. 228, pp. 217–227). Geological Society of America. https://doi.org/10.1130/SPE228-p217

Lang, H. M., Wachter, A. J., Peterson, V. L., & Ryan, J. G. (2004). Coexisting clinopyroxene/spinel and amphibole/spinel symplectites in metatroctolites from the Buck Creek ultramafic body, North Carolina Blue Ridge. *American Mineralogist*, *89*(1), 20–30. https://doi.org/10.2138/am-2004-0104

Larabee, D. (1966). Map showing distribution of ultramafic and intrusive mafic rocks from northern New Jersey to Alabama (IMAP 476). https://doi.org/10.3133/i476

Lee, J., & Jung, H. (2015). Lattice-preferred orientation of olivine found in diamond-bearing garnet peridotites in Finsch, South Africa and implications for seismic anisotropy. *Journal of Structural Geology*, *70*, 12–22. https://doi.org/10.1016/j.jsg.2014.10.015

Lloyd, G. E., Farmer, A. B., & Mainprice, D. (1997). Misorientation analysis and the formation and orientation of subgrain and grain boundaries. *Tectonophysics*, *279*(1–4), 55–78. https://doi.org/10.1016/S0040-1951(97)00115-7

Mainprice, D., Bachmann, F., Hielscher, R., & Schaeben, H. (2014). Descriptive tools for the analysis of texture projects with large datasets using MTEX: Strength, symmetry and components. *Geological Society, London, Special Publications*, *409*(1), 251–271. https://doi.org/10.1144/SP409.8

McElhaney, S., & McSween, H. J. (1983). Petrology of the Chunky Gal Mountain mafic-ultramafic complex, North Carolina. *Geological Society of America Bulletin*, *94*(7), 855–874. https://doi.org/10.1130/0016-7606(1983)94<855:POTCGM>2.0.CO;2

Mennenga, M. (2024). mennengam/RexRelict_Olivine: RexRelict_Olivine (2021) (Version Publish_2024) [Computer software]. *Zenodo*. https://doi.org/10.5281/ZENODO.13840873

Michels, Z. D., Kruckenberg, S. C., Davis, J. R., & Tikoff, B. (2015). Determining vorticity axes from grain-scale dispersion of crystallographic orientations. *Geology*, *43*(9), 803–806. https://doi.org/10.1130/G36868.1

Misra, K. C., & Keller, F. B. (1978). Ultramafic bodies in the southern Appalachians; a review. *American Journal of Science*, *278*(4), 389–418. https://doi.org/10.2475/ajs.278.4.389

Mizukami, T., Wallis, S. R., & Yamamoto, J. (2004). Natural examples of olivine lattice preferred orientation patterns with a flow-normal a-axis maximum. *Nature*, *427*(6973), 432–436. https://doi.org/10.1038/nature02179

Moecher, D. P., Samson, S. D., & Miller, C. F. (2004). Precise time and conditions of peak Taconian granulite facies metamorphism in the southern Appalachian orogen, USA, with implications for zircon behavior during crustal melting events. *The Journal of Geology*, *112*(3), 289–304. https://doi.org/10.1086/382760

Nicolas, A., Boudier, F., & Boullier, A. (1973). Mechanisms of flow in naturally and experimentally deformed peridotites. *American Journal of Science*, *273*(10), 853–876. https://doi.org/10.2475/ajs.273.10.853

Peterson, V., & Ryan, J. G., & 1997–1998 Research Experiences for Undergraduates (REU) Site Program Participants. (2009). Petrogenesis and structure of the Buck Creek mafic-ultramafic suite, southern Appalachians: Constraints on ophiolite evolution and emplacement in collisional orogens. *Geological Society of America Bulletin*, *121*(3–4), 615–629. https://doi.org/10.1130/B26302.1

Peterson, V. L., Rahl, J. M., DeYoung, S., Eyth, D., Mennenga, M., & Pummell, B. A. (2025). B-type olivine fabrics within the cumulate Buck Creek Ultramafic body emplaced during Southern Appalachian Taconic subduction, Version 1.0. *Interdisciplinary Earth Data Alliance (IEDA)*. https://doi.org/10.60520/IEDA/113466

Précigout, J., & Hirth, G. (2014). B-type olivine fabric induced by grain boundary sliding. *Earth and Planetary Science Letters*, *395*, 231–240. https://doi.org/10.1016/j.epsl.2014.03.052

Raymond, L. A., Swanson, S. E., Love, A. B., & Allan, J. F. (2003). Cr-spinel compositions, metadunite petrology, and the petrotectonic history of Blue Ridge ophiolites, Southern Appalachian Orogen, USA. *Geological Society, London, Special Publications*, *218*(1), 253–278. https://doi.org/10.1144/GSL.SP.2003.218.01.14

Skemer, P., Katayama, I., & Karato, S. (2006). Deformation fabrics of the Cima di Gagnone peridotite massif, Central Alps, Switzerland: Evidence of deformation at low temperatures in the presence of water. *Contributions to Mineralogy and Petrology*, *152*(1), 43–51. https://doi.org/10.1007/s00410-006-0093-4

Tasaka, M., Michibayashi, K., & Mainprice, D. (2008). B-type olivine fabrics developed in the fore-arc side of the mantle wedge along a subducting slab. *Earth and Planetary Science Letters*, *272*(3–4), 747–757. https://doi.org/10.1016/j.epsl.2008.06.014

Tenthorey, E., Ryan, J. G., & Snow, E. (1996). Petrogenesis of sapphirine-bearing metatroctolites from the Buck Creek ultramafic body, southern Appalachians. *Journal of Metamorphic Geology*, *14*(2), 103–114. https://doi.org/10.1046/j.1525-1314.1996.05793.x

Van der Wal, D., Chopra, P., Drury, M., & Gerald, J. F. (1993). Relationships between dynamically recrystallized grain size and deformation conditions in experimentally deformed olivine rocks. *Geophysical Research Letters*, *20*(14), 1479–1482. https://doi.org/10.1029/93GL01382

Van Ess, J., & Peterson, G. (2018). Exploring methods to determine the strain ellipsoid in dunites to provide context for EBSD CPO patterns. *Geological Society of America Abstracts with Programs*, *50*, 4. https://doi.org/10.1130/abs/2018NC-311977

Vollmer, F. (2018). Automatic contouring of geologic fabric and finite strain data on the unit hyperboloid. *Computers & Geosciences*, *115*, 134–142. https://doi.org/10.1016/j.cageo.2018.03.006

Warren, J. M., Hirth, G., & Kelemen, P. B. (2008). Evolution of olivine lattice preferred orientation during simple shear in the mantle. *Earth and Planetary Science Letters*, *272*(3–4), 501–512. https://doi.org/10.1016/j.epsl.2008.03.063

Webber, C., Newman, J., Holyoke, C. W., III., Little, T., & Tikoff, B. (2010). Fabric development in cm-scale shear zones in ultramafic rocks, Red Hills, New Zealand. *Tectonophysics*, *489*(1–4), 55–75. https://doi.org/10.1016/j.tecto.2010.04.001

Webber, C. E., Little, T., Newman, J., & Tikoff, B. (2008). Fabric superposition in upper mantle peridotite, Red Hills, New Zealand. *Journal of Structural Geology*, *30*(11), 1412–1428. https://doi.org/10.1016/j.jsg.2008.08.002

Wheeler, J., Piazolo, S., Prior, D. J., Trimby, P. W., & Tielke, J. A. (2024). Using crystal-lattice distortion data for geological investigations: The weighted Burgers vector method. *Journal of Structural Geology*, *179*, 105040. https://doi.org/10.1016/j.jsg.2023.105040

Wieser, P. E., Edmonds, M., Maclennan, J., & Wheeler, J. (2020). Microstructural constraints on magmatic mushes under Kīlauea Volcano, Hawai'i. *Nature Communications*, *11*(1), 14. https://doi.org/10.1038/s41467-019-13635-y

Woodcock, N. (1977). Specification of fabric shapes using an eigenvalue method. *Geological Society of America Bulletin*, *88*(9), 1231–1236. https://doi.org/10.1130/0016-7606(1979)90<310:SOFSUA>2.0.CO;2

Yao, Z., Qin, K., Wang, Q., & Xue, S. (2019). Weak B-type olivine fabric induced by fast compaction of crystal mush in a crustal magma reservoir. *Journal of Geophysical Research: Solid Earth*, *124*(4), 3530–3556. https://doi.org/10.1029/2018JB016728